Ionics (2024) 30:5353–5359
https://doi.org/10.1007/s11581-024-05660-9

RESEARCH

Ultrathin porous carbon nanosheets with enhanced surface energy storage for high-performance sodium-ion batteries

Jingyuan Huang[1] · Zhiqiang Zhang[1] · Shilin Yun[1] · Yuxin Diao[1] · Chuankun Zhang[2] · Hai-Chao Chen[1]

Received: 26 February 2024 / Revised: 11 June 2024 / Accepted: 22 June 2024 / Published online: 2 July 2024

Abstract

Carbon materials have long been the primary electrode materials for a series of electrochemical devices, but their applications for sodium-ion batteries (SIBs) are still restricted by limited embedding pathways between narrow graphene layers owing to relatively large size of Na^+. Here, the narrow interlayer issue is circumvented by enlarging the surface active sites of carbon materials, and the SIB performance is significantly promoted owing to enhanced surface energy storage. To provide more active areas and reduced ion diffusion distance, carbon nanosheets (CNSs) with ultrathin overall structure and highly porous microstructure were prepared by direct pyrolysis of potassium citrate. Potassium species serve as templates and activation agent for organic species carbonization and activation. The CNS exhibits an ultrahigh-specific surface area of 2062.7 $m^2\ g^{-1}$ due to its rich porous structure and two-dimensional nanosheet structure. These characteristics make our CNSs have numerous defects and active sites, as well as the reduced diffusion path for sodium-ion diffusion. CNS-700 also shows excellent energy storage performance as electrode material of SIBs. When used as an anode material, the CNS-700 exhibits a reversible capacity of 230 $mA\ h\ g^{-1}$ when cycled at 0.3 $A\ g^{-1}$ for 550 cycles. Furthermore, the CNS-700 displays a capacity of 175 $mA\ h\ g^{-1}$ when the current increases to 2 $A\ g^{-1}$.

Keywords Sodium-ion batteries · Porous carbons · Anode materials · Carbon nanosheets · Electrochemical energy storage

Introduction

With the ever-increasing utilization of renewable energy, there is a growing demand for high-performance and low-cost electrochemical batteries for large-scale power storage [1–5]. Due to the sufficient production of sodium and the low cost of mining, sodium-ion batteries (SIBs) are considered an ideal choice after lithium-ion batteries (LIBs) [6–9]. However, the relatively larger ion radius of Na^+ (0.102 nm) results in limited reaction kinetics and restricts the exploration of advanced sodium insertion materials [10, 11]. Carbon materials have long been the primary electrode materials for energy storage owing to their resource abundance, low cost, high electrical conductivity, and being environmentally friendly, which are also considered as promising candidates for SIB anode materials. However, a common anode material, commercial graphite carbon (theoretical LiC_6 capacity of 372 $mA\ h\ g^{-1}$ as the LIB anode), provides only 31 $mA\ h\ g^{-1}$ of practical capacity in SIBs owing to the fact that large atomic size of Na^+ limits the embedding pathways between narrow graphene layers [12–14]. Both theoretical calculations and experimental results show a greatly reduced Na^+ insertion energy barrier when the carbon interlayer distance is enlarged to 0.37 nm [15–17]. Therefore, enormous efforts have been made to enlarge the carbon interlayers for improved SIB performance. Saroja et al. [16] found that expanded interlayers of carbon nanotubes provide sufficient active sites for Na^+ adsorption and intercalation, and reaching 510 $mA\ h\ g^{-1}$ at 20 $mA\ g^{-1}$. Xu et al. [18] reported nitrogen-doped porous carbon nanosheets while pyrrolic nitrogen increased the interlayer distance of carbon

✉ Chuankun Zhang
zhangchk_lx@huat.edu.cn

✉ Hai-Chao Chen
chenhc@qdu.edu.cn

[1] Institute of Materials for Energy and Environment, School of Materials Science and Engineering, Qingdao University, Qingdao 266071, China

[2] Hubei Key Laboratory of Energy Storage and Power Battery, School of Mathematics, Physics and Optoelectronic Engineering, Hubei University of Automotive Technology, Shiyan 442002, China

expanding from 0.429 to 0.487 nm; as a result, a superb capacity of 294.1 mA h g^{-1} could be achieved at 0.1 A g^{-1}.

In addition to the internal crystal plane expansion of carbon, increasing the surface area can enhance surface-related energy storage and circumvent the narrow interlayer issue owing to more surface active sites and reduced ion diffusion distance. Therefore, proper structure construction for a large surface area provides a shortcut for performance optimization of carbon-based SIB anode materials. However, traditional porous carbons are fabricated as large granular particles with tortuous and narrow pores, which is unfavorable for fast Na^+ storage owing to unsatisfactory ion diffusion kinetics and limited available surface. 2D porous carbon nanosheets (CNSs) have the merits of a higher surface-to-volume ratio and more penetrated pores than traditional porous carbons [19–23], which have very potential to overcome the shortcomings of traditional porous carbon as SIB anode materials. However, the preparation of well-defined porous CNSs for SIB applications is still very challenging. Despite many specially designed strategies have been developed for preparing CNSs, such as biomass activation method [24, 25], organic molecular/salt blend pyrolysis [26], hard template method [27], pyrolysis of two-dimensional precursors [28], and self-assembly [29]; these methods need multiple steps with lengthy and complex process and expensive raw materials, and visible CNSs are aggregated together owing to non-uniform templating effect. Furthermore, additionally, added activation agents cannot activate the CNSs uniformly owing to their heterogeneous distribution, resulting in a limited specific area. Therefore, it is essential to develop efficient and high-quality CNS synthesis strategies to achieve better SIB performance.

Here, well-defined porous CNSs with large aspect ratios and uniformly activated pores were prepared by one-step pyrolysis of potassium citrate, and they were used as anode materials for SIBs. The organic part of potassium citrate could be used as a carbon source, and coordinated potassium could serve as both templating and activation agents. Using potassium citrate as a precursor ensured the uniform mixing of potassium with the carbon source at the molecule level, and this specific merit could result in a uniform templating effect for carbon assembly and then the uniform activation of assembled CNS, so our synthesis method had more merits compared to traditional synthesis methods. As a result, our CNS samples exhibited a homogenous nanosheet structure with a large aspect ratio and thin thickness, uniformly activated pores, and an ultrahigh-specific area of 2062.7 m^2 g^{-1}. Such a structure could provide more active sites and shorten ion diffusion distance for Na^+, resulting in increased capacity and rate performance.

Results and discussion

Figure 1 illustrates the formation mechanism for the CNSs synthesized at different temperatures. Potassium citrate was pyrolyzed in an argon atmosphere for the formation of CNSs. The inclusion of potassium species was very significant for generating 2D porous nanosheets. First, K_2CO_3 particles were formed as templates for organic species assembly at a low temperature (< 650 ℃), and 2D CNSs could be formed when pyrolysis and carbonization of the organic species at an elevated temperature. Meanwhile, CO_2 and K_2O species produced by thermal decomposition of K_2CO_3 ($K_2CO_3 \rightarrow K_2O + CO_2$) both react with preformed CNSs ($CO_2 + C \rightarrow 2CO$, $K_2O + C \rightarrow 2\,K + CO$), constructing a porous structure. Compared to the conventional synthesis method for activated carbon, our synthesis method had the following merits: first, the CNS was prepared by one annealing step without an extra addition of templating and activation agents that are commonly used, which could reduce the synthesis cost; second, templating effect of potassium species in the carbonization process was determinative for the 2D nanosheet formation; however, conventional method added the potassium species after carbonization and could not form a 2D nanosheets structure like our CNSs; third, potassium citrate was a typical organic-inorganic hybrid material, which ensured a uniform distribution of potassium

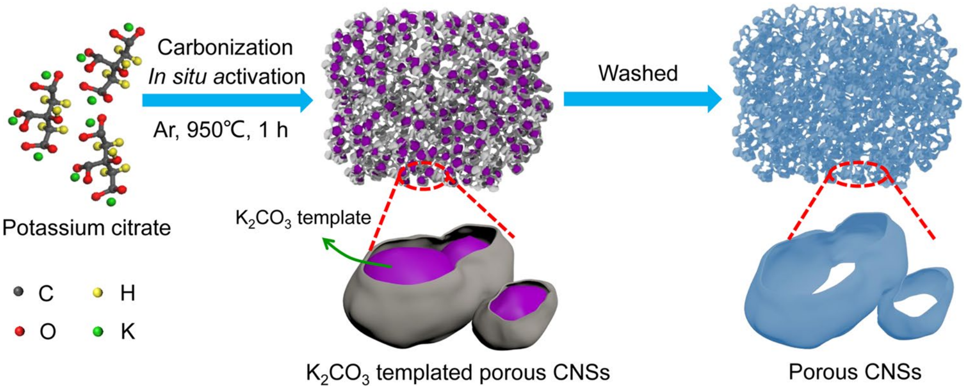

Fig. 1 Schematic of fabrication process and formation mechanism for the porous CNSs

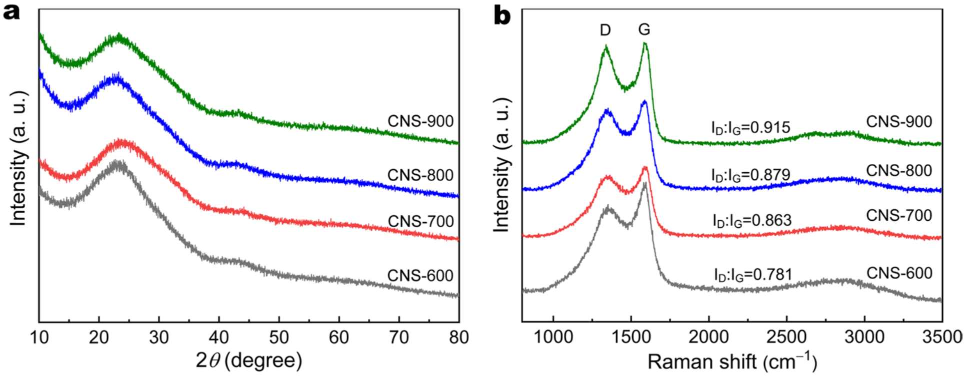

Fig. 2 **a** XRD patterns and **b** Raman spectra of the CNSs synthesized at different temperatures

species in carbon sources and resulted in uniform activation of the CNSs. Note that the activation process could be affected by pyrolysis temperature, forming different porous architectures. To this end, the annealing temperature was tuned for the optimized performance of CNSs.

Figure 2a shows the XRD patterns of these CNSs. There were two broad diffraction peaks located around 23° and 44°, which was a typical feature of amorphous porous carbon [30]. Raman spectra shown in Fig. 2b of these CNS samples all displayed two peaks at 1340 and 1585 cm^{-1}, which could be ascribed to D and G bands of carbonaceous materials. The D band was derived from the band edge A_{1g} mode, indicating that sp^2 carbon has a disordered structure or defects, and the G-band is related to the strain effect of E_{2g} mode. The calculated value of I_D/I_G was used to estimate the disorder degree or the number of defects in carbon materials. The I_D/I_G values gradually increased when the reaction temperature ascended from 600 to 900 ℃, indicating more defects formed with the increasing pyrolysis temperature [31]. Figure 3a shows the FESEM image of the CNS-700. It was obvious that the sample consisted of a large number of carbon nanosheets, and they interconnected to form a foam structure. This specific carbon foam structure could verify the templating effect of potassium species. High-resolution FESEM in Fig. 3b demonstrated uniform thickness of CNS around 30 nm, and the TEM image could verify the uniform thickness of the whole nanosheet (Fig. S1). In addition, the TEM image shown in Fig. 3c verified the uniform activation of the CNS-700, and many microspores could be found uniformly distributed in the CNS-700.

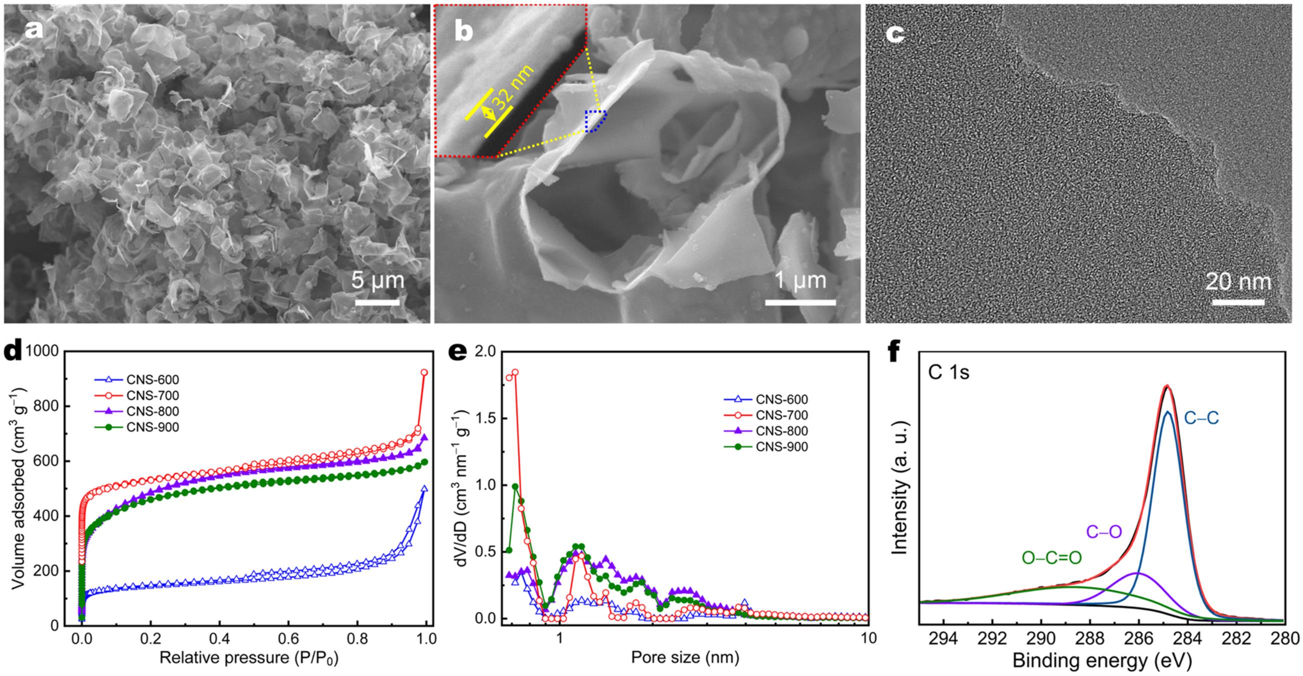

Fig. 3 **a**, **b** FESEM and **c** TEM images of the CNS-700. **d** N_2 adsorption/desorption isotherms and **e** pore size distribution curves of the CNS samples synthesized at different temperatures. **f** High-resolution XPS spectra for carbon element of the CNS-700

The porous structure of these CNS samples was also investigated using the nitrogen physical adsorption method to understand their porous structures. Huge nitrogen adsorption/desorption at the P/P_0 lower than 0.3 is a typical feature of a type I isotherm, indicating the existence of micropores. In addition, the hysteresis loop in the high P/P_0 region could be ascribed to a type IV isotherm owing to the existence of mesopores. As shown in Fig. 3d, the CNS-700 displayed larger N_2 adsorption than the other CNS samples, indicating the largest specific area. Especially, the CNS-700 shows huge N_2 uptake at relative pressure lower than 0.02 owing to a great deal of micropores, and its isotherm maintains a hysteresis loop in the P/P_0 region greater than 0.45 from the mesopores. The pore size distribution curve in Fig. 3e could verify the microporous structure of these CNS samples. The CNS-700 exhibited a high Brunauer-Emmett-Teller (BET) area of 2062.7 $m^2\ g^{-1}$, which is larger than the CNS-600 (531.6 $m^2\ g^{-1}$), CNS-800 (1690.5 $m^2\ g^{-1}$), and CNS-900 (1603.7 $m^2\ g^{-1}$) samples, and those reported porous carbons [32–43]. Greatly increased surface area of CNS-700 compared to CNS-600 is indicative of the activation of carbon which happened at a temperature of 700 ℃. Meanwhile, the CNS samples exhibited total pore volumes of 0.77, 1.00, 0.96, and 0.93$cm^3\ g^{-1}$ for CNS-600, CNS-700, CNS-800, and CNS-900, respectively. The largest BET area and total pore volumes of our CNS-700 could verify a highly porous structure of CNS-700. The CNS-700 was also characterized by XPS to show its elemental composition and chemical state of each element. The CNS-700 had a high purity and it exhibited the elemental signals of C and O in the wide-scan spectrum (Fig. S2). Peaks at 284.8 eV and 532.0 eV could be attributed to the XPS signals from C 1 s and O 1 s photoelectrons, respectively. Therefore, the CNS samples also maintained many residual oxygenated functional groups. The chemical states of elements in CNS-700 were further investigated by collecting high-resolution XPS spectra. The C-O and C = O signals were clearly visible in the

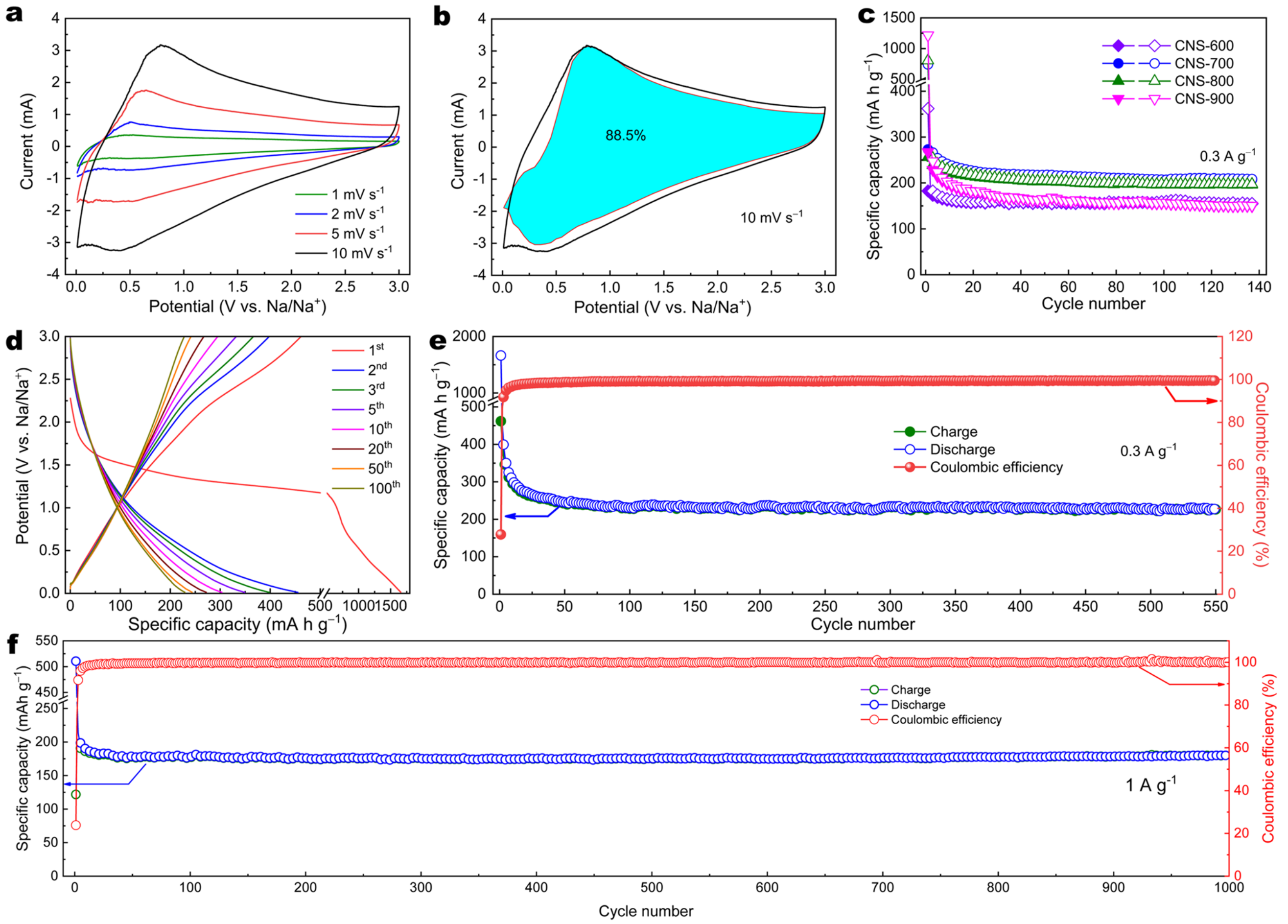

Fig. 4 **a** CV curves at various scan rates from 1 to 10 mV s^{-1} of CNS-700. **b** Separation of the surface-controlled and diffusion-controlled currents in the CV curve tested at a scan rate of 10 mV s^{-1}. **c** Cycling performance tested at 0.3 A g^{-1} for the CNS samples synthesized at different temperatures. **d** GCD curves at different cycles when cycled at 0.3 A g^{-1}, and long-term cycling performance and Coulombic efficiency of the CNS-700 when tested at specific currents of **e** 0.3 and (f) 1.0 A g^{-1}

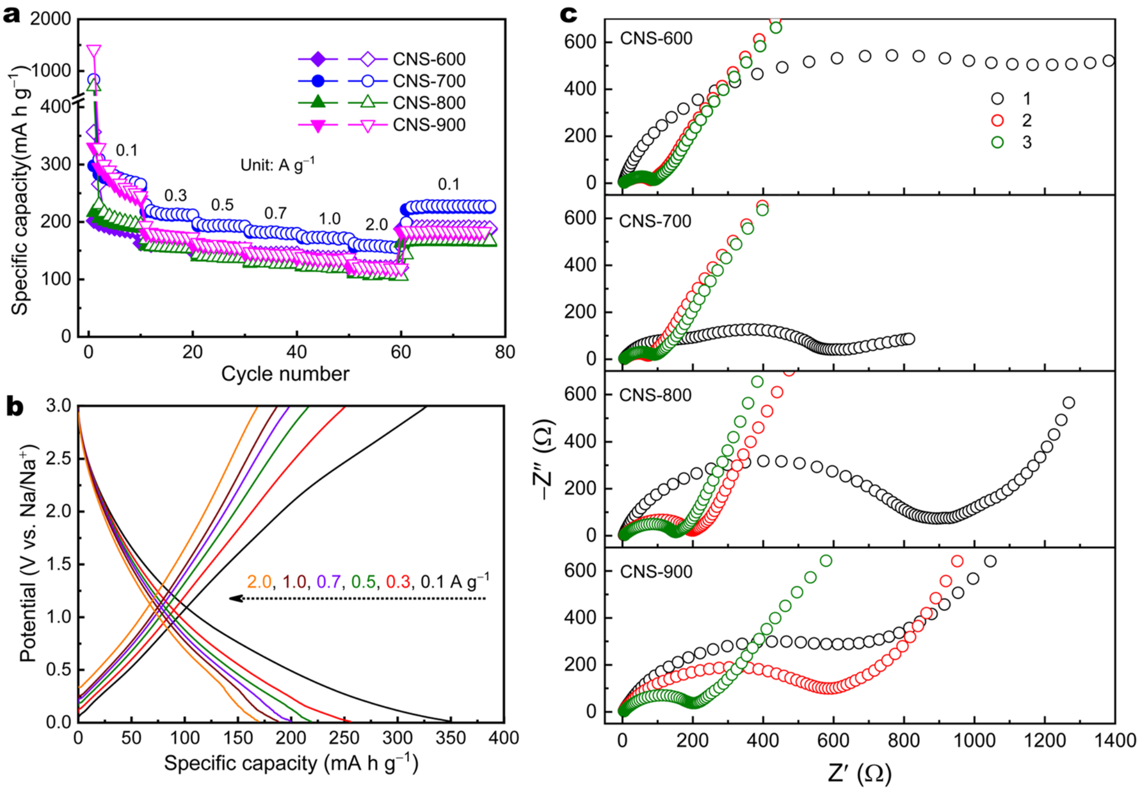

Fig. 5 **a** Rate performance of CNS samples synthesized at different temperatures, **b** GCD curves at different tested currents of CNS-700, and **c** EIS spectra of different CNS electrodes tested during different CV testing cycles with a scan rate of 0.3 mV s^{-1}: (1) fresh electrode, (2) after 3 cycles, and (3) after 8 cycles

high-resolution C 1 s spectrum, except for photoelectrons which come from C-C valence electrons, as shown in Fig. 3f.

Half batteries of SIBs were assembled using these CNS electrodes and their energy storage properties were first analyzed by a CV test. Figure 4a shows the CV curves of a CNS-700 electrode tested within the potentials of 0.01–3.0 V vs. Na/Na$^+$. It was found that the CV curves displayed the shape without obvious redox peaks, indicating surface-controlled energy storage owing to the high specific area of CNS-700. The surface-controlled contribution for energy storage was quantitatively analyzed using the relationship of $I = k_1 v + k_2 v^{0.5}$, [44, 45] and it found the energy storage of CNS-700 is mainly from the surface-controlled process (Fig. S3). As shown in Fig. 4b, 88.5% of the capacity is dominated by a surface-controlled process. The cycling stability of the CNS samples was evaluated by repeated charge/discharge test at 0.3 A g^{-1}. The CNS samples all exhibited relatively stable cycling stability after initial cycles (Fig. 4c). By comparing their capacities, it could be found that the CNS-700 electrode had the highest capacity than these CNS samples synthesized at other temperatures. The CNS-700 electrode had an initial discharge capacity of 720 mA h g^{-1} and a charging capacity of 270 mA h g^{-1}. After slight capacity reduction during the initial several cycles, the CNS-700 electrode remained stable charge/discharge capacity around 241.7/244.7 mA h g^{-1}. The capacity attenuation of the battery during the initial cycle could be attributed to the formation of SEI film and irreversible side reactions [46–48]. The GCD curves of the CNS-700 electrode at different cycles are plotted in Fig. 4d. After the initial cycle, the GCD curves of the CNS-700 electrode tended to be stable, indicating a stable performance. As shown in Fig. 4e and f, after cycling for more than 500 cycles at 0.3 A g^{-1} and 1000 cycles at 1.0 A g^{-1}, the CNS-700 electrode still remained at a capacity of 230 and 180 mA h g^{-1}, respectively. In addition, the CE are all higher than 99% after initial cycles. The C 1 s XPS spectra showed the appearance of carbide when the CNS-700 electrode experienced the charge/discharge cycle, but the XPS did not change when being cycled for 1000 cycles (Fig. S4). These results confirmed the excellent cycling stability of the CNS-700 electrode.

The rate performance of CNS electrodes is compared in Fig. 5a. After testing at stepped currents of 0.1, 0.3, 0.5, 0.7, 1.0, and 2.0 A g^{-1}, the CNS-700 electrode showed a charge/discharge capacity of 280/300 mA h g^{-1} at a specific current of 0.1 A g^{-1}, indicating high reversibility at different tested currents. The CNS-700 electrode could maintain a favorable discharge capacity of around 175/177 mA h g^{-1} at a high specific current of 2.0 A g^{-1}, indicating excellent rate performance. The CNS-700 electrode delivered a specific capacity obviously higher than a series of previously reported carbon-based electrode derived from different carbon precursors, such as Palmyra palm fruit calyx (245 mA h g^{-1} at 0.05 A g^{-1}) [49], sorghum stalk (212 mA h g^{-1} at 0.1 A g^{-1}) [50], lotus petioles (242 mA h g^{-1} at 0.1 A g^{-1}) [51], pistachio shell (225 mA h g^{-1} at 0.01 A g^{-1}) [52], sodium alginate (216 mA h g^{-1} at 0.1 A g^{-1}) [53], *Spartina alterniflora* (139 mA h g^{-1} at 0.1 A g^{-1}) [54], and corn stalks (249 mA h g^{-1} at 0.1 A g^{-1}) [55]. Figure 5b compares the typical GCD curves of CNS-700 electrode. These GCD curves exhibited similar shapes at different specific currents, further confirming a good rate performance. In addition, electrochemical impedance spectroscopy (EIS) was also used for evaluating the stability of different CNS electrodes. As shown in Fig. 5c, the EIS spectra of the CNS electrodes all displayed greatly reduced diameters of the semicircles in high frequency region after three CV cycles, indicating greatly reduced charge transfer resistance. However, only CNS-600 and CNS-700 electrodes show constant EIS spectra in subsequent CV cycles, so better stability for energy storage could be achieved at relatively low annealing temperature.

Conclusions

To circumvent the narrow interlayer issue for SIB application of carbon materials, 2D porous carbon nanosheets (CNSs) with large aspect ratio and very thin thickness were synthesized to boost the surface energy storage. The CNSs were prepared by direct pyrolysis of potassium citrate, where potassium species served as templates and activation agents for organic species carbonization and activation. The CNS exhibited an ultrahigh-specific surface area of 2062.7 m^2 g^{-1} due to its rich porous structure and two-dimensional nanosheet structure. These characteristics not only provided abundant defect sites and active sites, but also shortened the diffusion path of sodium ions. When used as an anode material, the CNS-bade SIB exhibited high reversible capacity and long-term cycling stability. Our work provided a solution for the limited capacity of carbon materials for SIB applications, which is very promising to promote the application of SIBs.

Supplementary information The online version contains supplementary material available at https://doi.org/10.1007/s11581-024-05660-9.

Author contributions Jingyuan Huang: Methodology, Investigation, Writing-Original Draft. Zhiqiang Zhang: Investigation, Validation. Shilin Yun: Validation, Data Curation. Yuxin Diao: Validation, Data Curation. Chuankun Zhang: Conceptualization, Methodology, Writing-Review & Editing. Hai-Chao Chen: Conceptualization, Methodology, Resources, Supervision, Writing-Review & Editing, Funding acquisition.

Funding This work is financially supported by the National Natural Science Foundation of China (no. 21905148), Open Project from Hubei Key Laboratory of Energy Storage and Power Battery, Hubei University of Automotive Technology (no. ZDK22023B02), and Hubei Provincial Natural Science Foundation of China (no. 2024AFD115).

Declarations

Competing interests The authors declare no competing interests.

References

1. Li H, He Y, Wang Q et al (2023) $SnSe_2$/$NiSe_2$@N-doped carbon yolk-shell heterostructure construction and selenium vacancies engineering for ultrastable sodium-ion storage. Adv Energy Mater 13:2302901
2. Zong Y, Chen H, Wang J et al (2023) Cation defect-engineered boost fast kinetics of two-dimensional topological Bi_2Se_3 cathode for high-performance aqueous Zn-ion batteries. Adv Mater 35:2306269
3. Liu B, Zhang Q, Li L et al (2019) Encapsulating red phosphorus in ultralarge pore volume hierarchical porous carbon nanospheres for lithium/sodium-ion half/full batteries. ACS Nano 13:13513–13523
4. Cao J, Hu Y, Zhu Y et al (2021) Synthesis of mesoporous nickel-cobalt-manganese sulfides as electroactive materials for hybrid supercapacitors. Chem Eng J 405:126928
5. Liao Y, Chen H-C, Yang C et al (2022) Unveiling performance evolution mechanisms of MnO_2 polymorphs for durable aqueous zinc-ion batteries. Energy Storage Mater 44:508–516
6. Liu Q, Hu Z, Li W et al (2021) Sodium transition metal oxides: the preferred cathode choice for future sodium-ion batteries? Energy Environ Sci 14(1):158–179
7. Yao T, Wang H, Ji X et al (2023) Introducing hybrid defects of silicon doping and oxygen vacancies into MOF-derived TiO_{2-x}@carbon nanotablets towards high-performance sodium-ion storage. Small 19:2302831
8. Dong C, Shao H, Zhou Y et al (2022) Construction of ZnS/Sb_2S_3 heterojunction as an ion-transport booster toward high-performance sodium storage. Adv Funct Mater 33:2211864
9. Yao T, Wang H, Qin Y, Shi JW, Cheng Y (2023) Enhancing pseudocapacitive behavior of MOF-derived TiO_{2-x}@carbon nanocubes via Mo-doping for high-performance sodium-ion capacitors. Compos B 253:11057
10. Cheng D-L, Yang L-C, Zhu M (2018) High-performance anode materials for Na-ion batteries. Rare Met 37(3):167–180
11. Peng J, Zhang W, Liu Q et al (2022) Prussian blue analogues for sodium-ion batteries: past, present, and future. Adv Mater 34(15):e2108384
12. Doeff MM, Ma Y, Visco SJ et al (1993) Electrochemical insertion of sodium into carbon. J Electrochem Soc 140(12):L169–L170
13. Stevens DA, Dahn JR (2001) The mechanisms of lithium and sodium insertion in carbon materials. J Electrochem Soc 148(8):A803
14. Luo W, Shen F, Bommier C et al (2016) Na-ion battery anodes: materials and electrochemistry. Acc Chem Res 49(2):231–240
15. Cao Y, Xiao L, Sushko ML et al (2012) Sodium ion insertion in hollow carbon nanowires for battery applications. Nano Lett 12(7):3783–3787
16. Vijaya Kumar Saroja AP, Muruganathan M, Muthusamy K et al (2018) Enhanced sodium ion storage in interlayer expanded multiwall carbon nanotubes. Nano Lett 18(9):5688–5696
17. Yang Y, Tang D-M, Zhang C et al (2017) "Protrusions" or "holes" in graphene: which is the better choice for sodium ion storage? Energy Environ Sci 10(4):979–986
18. Xu C, Yang W, Ma G et al (2022) Edge-nitrogen enriched porous carbon nanosheets anodes with enlarged interlayer distance for fast charging sodium-ion batteries. Small 18:2204375

19. Ma C, Fan Q, Dirican M et al (2020) Porous carbon nanosheets derived from expanded graphite for supercapacitors and sodium-ion batteries. J Mater Sci 55(34):16323–16333
20. Yoon D, Kim DH, Chung KY et al (2016) Hydrogen-enriched porous carbon nanosheets with high sodium storage capacity. Carbon 98:213–220
21. Wen Y, Wen X, Wenelska K et al (2019) Novel strategy for preparation of highly porous carbon sheets derived from polystyrene for supercapacitors. Diam Relat Mater 95:5–13
22. Sun F, Wang K, Wang L et al (2019) Hierarchical porous carbon sheets with compressed framework and optimized pore configuration for high-rate and long-term sodium and lithium ions storage. Carbon 155:166–175
23. Subburam G, Ramachandran K, El-Khodary SA et al (2021) Development of porous carbon nanosheets from polyvinyl alcohol for sodium-ion capacitors. Chem Eng J 415:129012
24. Hou J, Jiang K, Tahir M et al (2017) Tunable porous structure of carbon nanosheets derived from puffed rice for high energy density supercapacitors. J Power Sources 371:148–155
25. Mondal AK, Kretschmer K, Zhao Y et al (2017) Nitrogen-doped porous carbon nanosheets from eco-friendly eucalyptus leaves as high performance electrode materials for supercapacitors and lithium ion batteries. Chem-Eur J 23(15):3683–3690
26. Liu B, Yang M, Chen H et al (2018) Graphene-like porous carbon nanosheets derived from salvia splendens for high-rate performance supercapacitors. J Power Sources 397:1–10
27. Zhang Y, Fan W, Lu H et al (2018) Highly porous polyimide-derived carbon aerogel as advanced three-dimensional framework of electrode materials for high-performance supercapacitors. Electrochim Acta 283:1763–1772
28. Zhao K, Liu S, Ye G et al (2018) High-yield bottom-up synthesis of 2D metal–organic frameworks and their derived ultrathin carbon nanosheets for energy storage. J Mater Chem A 6(5):2166–2175
29. Wang J, Chen S, Deng H et al (2019) Simple synthesis of porous carbon sheet by reduction reaction of in-situ formed carbon dioxide for supercapacitor application. Results Phys 12:1340–1343
30. Yin X, Zhao Y, Wang X et al (2022) Modulating the graphitic domains of hard carbons derived from mixed pitch and resin to achieve high rate and stable sodium storage. Small 18(5):e2105568
31. Yan J, Li H, Wang K et al (2021) Ultrahigh phosphorus doping of carbon for high-rate sodium ion batteries anode. Adv Energy Mater 11(21):2003911
32. Wang S, Xia L, Yu L et al (2016) Free-standing nitrogen-doped carbon nanofiber films: integrated electrodes for sodium-ion batteries with ultralong cycle life and superior rate capability. Adv Energy Mater 6(7):1502217
33. Wang M, Yang Z, Li W et al (2016) Superior sodium storage in 3D interconnected nitrogen and oxygen dual-doped carbon network. Small 12(19):2559–2566
34. Li Y, Hu Y-S, Titirici M-M et al (2016) Hard carbon microtubes made from renewable cotton as high-performance anode material for sodium-ion batteries. Adv Energy Mater 6(18):1600659
35. Cao B, Liu H, Xu B et al (2016) Mesoporous soft carbon as an anode material for sodium ion batteries with superior rate and cycling performance. J Mater Chem A 4(17):6472–6478
36. Zou G, Wang C, Hou H et al (2017) Controllable interlayer spacing of sulfur-doped graphitic carbon nanosheets for fast sodium-ion batteries. Small 13(31):1700762
37. Zhang F, Yao Y, Wan J et al (2017) High temperature carbonized grass as a high performance sodium ion battery anode. ACS Appl Mater Interfaces 9(1):391–397
38. Liu H, Jia M, Yue S et al (2017) Creative utilization of natural nanocomposites: nitrogen-rich mesoporous carbon for a high-performance sodium ion battery. J Mater Chem A 5(20):9572–9579
39. Hou H, Shao L, Zhang Y et al (2017) Large-area carbon nanosheets doped with phosphorus: a high-performance anode material for sodium-ion batteries. Adv Sci 4(1):1600243
40. Lu P, Sun Y, Xiang H et al (2018) 3D amorphous carbon with controlled porous and disordered structures as a high-rate anode material for sodium-ion batteries. Adv Energy Mater 8(8):1702434
41. Feng Y, Tao L, He Y et al (2019) Chemical-enzymatic fractionation to unlock the potential of biomass-derived carbon materials for sodium ion batteries. J Mater Chem A 7(47):26954–26965
42. Kim D-Y, Li OL, Kang J (2020) Novel synthesis of highly phosphorus-doped carbon as an ultrahigh-rate anode for sodium ion batteries. Carbon 168:448–457
43. Xu T, Qiu X, Zhang X et al (2023) Regulation of surface oxygen functional groups and pore structure of bamboo-derived hard carbon for enhanced sodium storage performance. Chem Eng J 452:139514
44. Liu B, Zhang Q, Li L et al (2021) Close-packed storage of potassium metallic clusters achieved through nanostructure engineering of ultrafine hollow nanoparticles-based carbon nanoclusters. EcoMat 3:e12105
45. Jiang S, Yun S, Cao H et al (2022) Porous carbon matrix-encapsulated MnO in situ derived from metalorganic frameworks as advanced anode materials for Li-ion capacitors. Sci China Mater 65(1):59–68
46. Zhang Y, Bi Z, Liang Y et al (2022) Ultrahigh line-capacity and flexible graphene/carbon nanotube/tin oxide fibers as sodium ion battery anodes. Energy Storage Mater 48:35–43
47. Wan Y, Liu Y, Chao D, Li W, Zhao D (2023) Recent advances in hard carbon anodes with high initial Coulombic efficiency for sodium-ion batteries. Nano Mater Sci 5:189–201
48. Jiang S, Huang C, Zhang Z et al (2023) Combined contributions from multidimensional micropores and mesopores of hierarchical porous carbons for extraordinary Li-ion storage applications. Carbon 214:118390
49. Damodar D, Ghosh S, Usha Rani M et al (2019) Hard carbon derived from sepals of Palmyra palm fruit calyx as an anode for sodium-ion batteries. J Power Sources 438:227008
50. Zhu X, Jiang X, Liu X et al (2017) A green route to synthesize low-cost and high-performance hard carbon as promising sodium-ion battery anodes from sorghum stalk waste. Green Energy Environ 2(3):310–315
51. Wang P, Qiao B, Du Y et al (2015) Fluorine-doped carbon particles derived from lotus petioles as high-performance anode materials for sodium-ion batteries. J Phys Chem C 119(37):21336–21344
52. Kim K, Lim DG, Han CW et al (2017) Tailored carbon anodes derived from biomass for sodium-ion storage. ACS Sustain Chem Eng 5(10):8720–8728
53. Hu H, Cao L, Xu Z et al (2016) Carbon nanosheet frameworks derived from sodium alginate as anode materials for sodium-ion batteries. Mater Lett 185:530–533
54. Cheng H, Tang Z, Luo X et al (2021) Spartina alterniflora-derived porous carbon using as anode material for sodium-ion battery. Sci Total Environ 777:146120
55. Ou J, Zhang H, Wang H et al (2021) Corn stalks derived hierarchical porous carbon as ultra-efficient anode materials for sodium-ion batteries. Diam Relat Mater 120:108626